

Efficient Wideband DoA Estimation with a Robust Iterative Method in UCA-based MIMO Systems

Xiaorui Ding, Wenbo Xu, *Member, IEEE*, Yue Wang, *Senior Member, IEEE*

Abstract

In multiple-input multiple-output systems, direction-of-arrival (DoA) estimation is a critical technique as the basis of precoding and beamforming. With the ever-increasing requirement of high data rate and ubiquitous devices, effective wideband DoA estimation is desirable. In this paper, we propose an iterative coherent signal-subspace method including three steps in each iteration for two-dimensional (2D) DoA estimation with a uniform circular array. The first step selects partial frequency points for the subsequent focusing process to reduce unnecessary complexity. The second step realizes the focusing process, where we provide angle intervals to generate focusing matrices with robustness, and the signal-subspaces at the selected frequency points are focused into a reference frequency. The third step estimates DoAs with the multiple signal classification algorithm where the range of the spatial spectrum is constrained by the aforementioned angle intervals, thereby further reducing the complexity. The key parameters of the proposed method in the current iteration are adjusted based on the previous estimation results. In addition, we derive the Cramér-Rao bound of the investigated wideband 2D DoA estimation to provide guidance for practical applications. The simulation results indicate that our proposed method enjoys better performance and implementation efficiency when compared with benchmark methods.

Index Terms

Cramér-Rao bound, direction-of-arrival estimation, iterative coherent signal-subspace method, multiple-input multiple-output systems, uniform circular array.

I. INTRODUCTION

In wireless communication systems, multiple-input multiple-output (MIMO) has been widely used for improving the spectral efficiency and the communication reliability. Various techniques have been applied in MIMO systems, where direction-of-arrival (DoA) estimation is an important

This work was supported in part by the National Natural Science Foundation of China under Grant 61871050 and the US National Science Foundation under Grant 2136202.

X. Ding and W. Xu are with the Key Lab of Universal Wireless Communications, Ministry of Education, Beijing University of Posts and Telecommunications.

Y. Wang is with the Department of Electrical and Computer Engineering, George Mason University, Fairfax, VA.

W. Xu (e-mail: xuwb@bupt.edu.cn) and Y. Wang (e-mail: ywang56@gmu.edu) are the corresponding authors.

one that estimates the DoAs of signal sources. This technique acts as the foundation of precoding and beamforming [1]–[3], which effectively eliminate the interference and noise, and increase the data rate [4] of communication systems.

Among different types of antenna arrays, the uniform circular array (UCA) is popular in MIMO systems since its beam shape does not change with the azimuth directions [5], which can improve the reliability of precoding and beamforming under different azimuths. Such benefit attracts many scholars to investigate the DoA estimation in UCA-based MIMO systems, and the effective methods such as the maximum-likelihood (ML) method [6], the multiple signal classification (MUSIC) algorithm [7], estimating signal parameters via rotational invariance techniques (ESPRIT) [8] and some deep-learning-based methods [9]–[11] are developed for estimating DoAs with UCA. These methods achieve different trade-offs between performance and complexity, thereby satisfying the demands of various scenarios.

MUSIC algorithm is the most popular one among these methods due to its excellent performance and reasonable complexity [12]–[14]. It utilizes eigenvalue decomposition (EVD) of the signal covariance matrix to construct the signal-subspace and the noise-subspace. Then, the DoAs of multiple signals are obtained through peak-searching in a spatial spectrum formed by the orthogonality of the two subspaces. Furthermore, when there are enough snapshots and the arriving signals are uncorrelated, the performance of MUSIC algorithm is close to that of ML method [12] which has perfect performance but suffers from heavy complexity burden.

Nonetheless, MUSIC algorithm is only suitable for the narrowband DoA estimation. Fortunately, some practical methods are investigated to estimate DoAs of wideband signals that are common in MIMO systems. For instance, incoherent signal-subspace method (ISM) transforms wideband signal-subspace into narrowband ones by Fourier transform [15]–[17]. Then ISM respectively performs narrowband DoA estimation method on each narrowband signal-subspaces and finally synthesizes the results. Alternatively, Jacobi-Anger approximation transforms all narrowband manifold matrices into a manifold matrix of a virtual uniform linear array, and then narrowband methods can be used to estimate DoAs [18]–[20].

Due to the multipath effect in MIMO systems, the wideband signals received by antenna arrays may be from different paths of the same signal with small time intervals, which are approximately coherent and hard for the aforementioned classic methods to estimate DoAs accurately. Considering such problem, [21] proposed the coherent signal-subspace method (CSM) with preferable performance for approximate coherent signals, which is based on coarse pre-

estimated DoAs. CSM refines these DoAs by MUSIC algorithm after focusing signal-subspaces at each frequency point into a reference frequency by focusing matrices. However, its performance is affected by the exactness of focusing matrices and the accuracy of pre-estimated DoAs.

To improve the performance of CSM, some methods have been proposed to construct more exact focusing matrices, including rotational signal-subspace (RSS) [22], signal-subspace transformation [23], two-sided correlation transformation [24], etc. Apart from these methods, some works adopt other strategies to further improve the performance of CSM. [22] presented the iteration mechanism and added extra angles for focusing, where the angles participated in focusing process are called focusing angles. Additionally, [25] proposed the robust CSM (R-CSM) that samples focusing angles from a robustness interval and iteratively estimates DoAs with CSM, so as to reduce the effect of unfavorable pre-estimated DoAs on estimation performance. [26] investigated the iterative CSM based on two-dimensional (2D) discrete Fourier transform (I-2D-CSM) to further improve the performance, which optimizes the robustness interval of R-CSM by setting a minimum radius for it. However, these methods are only designed for one-dimensional (1D) DoA estimation, and the robustness intervals of R-CSM and I-2D-CSM are introduced without refinement, which leads to high complexity.

In addition, Cramér-Rao bound (CRB) is a typical benchmark of DoA estimation performance, which indicates the lower bound of the variance of estimated DoAs [12]. Many works have derived the CRBs for UCA-based MIMO systems in various conditions in terms of the dimension of DoA, bandwidth, the number of signal sources, the number of snapshots and so on. For instance, [27] derived the CRB for 1D DoAs of narrowband signals with multiple snapshots, [8] derived the CRB for 2D DoAs of narrowband signals with multiple snapshots, and [28] derived the CRB for 2D DoAs of wideband signals with a single snapshot. However, the existing CRBs are not suitable for wideband 2D DoA estimation methods with UCA which requires multiple snapshots, e.g. CSM.

To achieve better performance than the aforementioned CSM methods [22], [25], [26] without introducing high computational complexity, we propose a wideband 2D DoA estimation method named robust iterative partial-focusing CSM (RIPF-CSM). Then, the CRB is derived to give guidance for corresponding wideband 2D DoA estimation. The main contributions of this paper are summarized as follows.

- 1) An efficient iterative 2D DoA estimation method called RIPF-CSM for UCA-based MIMO systems is proposed. In RIPF-CSM, the robustness intervals with less redundant focusing

angles are designed to improve the focusing performance and reduce computational complexity. In order to further accelerate the estimation procedure, the range of MUSIC spatial spectrum is shrunk and the number of candidate frequency points in focusing process is reduced. During the iterations, the parameters of the above designs are adjusted based on the previous estimated DoAs to improve the reliability.

- 2) The computational complexity of RIPF-CSM is analysed and compared with 2D DoA estimation version of the benchmark CSM methods, where these 2D versions are obtained by extending the corresponding 1D versions. The comparative results demonstrate the complexity of RIPF-CSM is more preferable among all discussed methods.
- 3) We develop the CRB of wideband 2D DoA estimation with UCA while considering multiple signal sources and multiple snapshots, which has not been presented in current literature to the best of our knowledge. According to the derived CRB analytical results, we provide effective guidelines for the practical implementation of the wideband 2D DoA estimation with UCA-based MIMO systems.

The rest of this paper is organized as follows. In Section II, we introduce the signal model and problem formulation for 2D DoA estimation with UCA. Then, the RIPF-CSM is proposed and its computational complexity is discussed in Section III. In Section IV, we develop the CRB of DoA estimation, based on which guidelines for practical implementation are provided. The simulation results are presented in Section V, followed by conclusions in Section VI.

Notations: In this paper, e denotes the natural constant. $j = \sqrt{-1}$ stands for the imaginary unit. $\mathbf{1}_M$ and \mathbf{I}_M respectively represent $M \times M$ all-ones matrix and $M \times M$ identity matrix. $\mathbb{R}^{M \times N}$ and $\mathbb{C}^{M \times N}$ stand for $M \times N$ real and complex matrices, respectively. $[\cdot]^{-1}$, $[\cdot]^T$ and $[\cdot]^H$ denote the inverse, transpose and conjugate transpose of a matrix, respectively. $|\cdot|$ stands for the absolute value of a scalar or the number of elements in a set, and $\|\cdot\|_F$ represents the Frobenius norm of a matrix. $\mathcal{E}[\cdot]$ denotes the expectation of a random variable. $\mathcal{P}[\cdot]$ stands for and the probability of a random variable. $\lceil \cdot \rceil$ and $\lfloor \cdot \rfloor$ represent the round-up and round-down operation, respectively. $\max[\cdot]$, $\min[\cdot]$ and $\min[\cdot|\mathcal{H}]$ stand for the largest number, the smallest number, and the smallest number with condition \mathcal{H} , respectively. $\arg \min[\cdot]$ obtains the optimal variable value that minimizes the expression in the bracket. $\text{diag}[\cdot]$ denotes a diagonal or block diagonal matrix, where the entries in the bracket respectively stand for the diagonal elements or blocks in order. $\text{trace}[\cdot]$ denotes the trace of a matrix. $\text{Re}[\cdot]$ and $\text{Im}[\cdot]$ represent the real and imaginary parts of a complex variable, respectively. \odot stands for Hadamard product. $\mathcal{O}(N)$ represents the

computational complexity which is less than CN operations as N tends to infinite, and C is a positive real number.

II. SIGNAL MODEL AND PROBLEM FORMULATION

In this section, we describe the signal receiving model of wideband 2D DoA estimation in UCA-based MIMO systems. Then, the conventional CSM is introduced to facilitate the subsequent presentation of our proposed method.

A. Signal Model

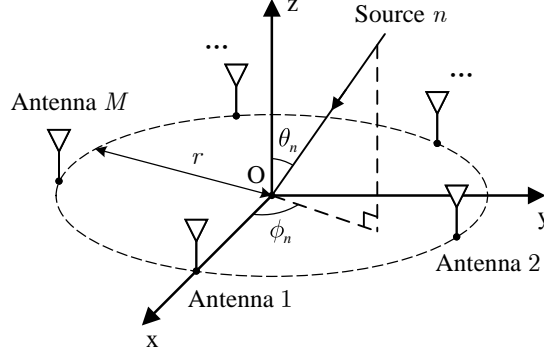


Fig. 1. Signal receiving geometry of UCA-based MIMO systems.

As shown in Fig. 1, we consider the MIMO receiver with a UCA equipped by M omnidirectional antenna elements in the x - y plane. Suppose there are N ($N < M$) far-field incident wideband signals from different directions with central frequency f_0 , and the arriving elevation and azimuth of the n -th signal source are respectively θ_n and ϕ_n , where $n \in \{1, 2, \dots, N\}$, $\theta_n \in [0^\circ, 90^\circ]$ and $\phi_n \in [0^\circ, 360^\circ)$. In order to ensure that the antenna array has no grid lobe [29], we suppose that the distance between adjacent antennas is no greater than the half of the minimum wavelength λ_{\min} of the received signals. Thus, denoting r as the radius of UCA, it can be derived from the geometric relations that $r \leq \lambda_{\min}/(4 \sin(\pi/M))$ [30].

With the sampling rate f_s which avoids the spectrum aliasing, the output samples of UCA are collected in the matrix $\mathbf{X}_t \in \mathbb{C}^{M \times K_t}$, where $K_t = \lfloor t_0 f_s \rfloor$ stands for the number of snapshots, and t_0 represents the sampling duration. The samples in each row of \mathbf{X}_t correspond to the analytic signals from the same antenna. Meanwhile, we suppose the noise in channels to be additive and obey white Gaussian distribution with zero mean and variance σ^2 .

Since the typical steering vector formulations are only valid for the narrowband signals [21]–[26], we transform \mathbf{X}_t to multiple narrowband signal matrices at different frequency points by performing fast Fourier transforms (FFTs) on K_f segments that are split from each row of \mathbf{X}_t , where the number of FFT points is defined as Z ($Z < K_t$) and $K_f = \lfloor K_t/Z \rfloor$ is the number of snapshots in frequency domain. The actual frequencies f_z of each frequency point can be easily calculated from f_0 , f_s and Z according to the Nyquist sampling theorem, where $z \in \{1, 2, \dots, Z\}$. We define the narrowband signal matrix at the frequency point f_z as $\mathbf{X}_f(f_z) \in \mathbb{C}^{M \times K_f}$ which is expressed as [21]–[26]:

$$\mathbf{X}_f(f_z) = \mathbf{A}(f_z, \mathbb{S})\mathbf{S}_f(f_z) + \mathbf{W}(f_z), \quad (1)$$

where \mathbb{S} is the set including all DoAs of signal sources, $\mathbf{A}(f_z, \mathbb{S}) = [\mathbf{a}(f_z, \theta_1, \phi_1), \mathbf{a}(f_z, \theta_2, \phi_2), \dots, \mathbf{a}(f_z, \theta_N, \phi_N)]$ is the manifold matrix, $\mathbf{a}(f_z, \theta_n, \phi_n)$ is the steering vector of the n -th signal source, $n \in \{1, 2, \dots, N\}$, $\mathbf{S}_f(f_z) \in \mathbb{C}^{N \times K_f}$ is the narrowband source signal matrix and $\mathbf{W}(f_z) \in \mathbb{C}^{M \times K_f}$ is the Gaussian noise matrix, respectively. The reference position of zero phase is regarded as the center of UCA. Accordingly, the steering vector of the n -th signal source is given as:

$$\mathbf{a}(f_z, \theta_n, \phi_n) = \left[e^{j \frac{2\pi r f_z}{c} \sin \theta_n \cos(\frac{2\pi \times 0}{M} - \phi_n)}, e^{j \frac{2\pi r f_z}{c} \sin \theta_n \cos(\frac{2\pi \times 1}{M} - \phi_n)}, \dots, e^{j \frac{2\pi r f_z}{c} \sin \theta_n \cos(\frac{2\pi(M-1)}{M} - \phi_n)} \right]^T, \quad (2)$$

where c represents the light speed. Based on the model in (1), the objective is to estimate the 2D DoAs from the narrowband signal matrices $\mathbf{X}_f(f_z)$, $z = 1, 2, \dots, Z$.

B. Conventional CSM

The conventional CSM is an effective DoA estimation method, which refines the coarse pre-estimated DoAs [21] acquired by some methods with low complexity, e.g., conventional beamforming (CBF) [31] and MUSIC algorithm with large search steps. The key step of CSM is the focusing process which transforms the signal-subspaces at different frequency points to the signal-subspace at a reference frequency. This process on narrowband signal matrix $\mathbf{X}_f(f_z)$ is expressed as:

$$\mathbf{R}_Y = \frac{1}{K_f Z^2} \sum_{z=1}^Z [\mathbf{B}(f_z) \mathbf{X}_f(f_z)] [\mathbf{B}(f_z) \mathbf{X}_f(f_z)]^H, \quad (3)$$

where \mathbf{R}_Y denotes the average covariance matrix of the focused narrowband signals, and $\mathbf{B}(f_z)$ denotes the focusing matrix at the frequency point f_z . Regarding f_0 as the reference frequency, $\mathbf{B}(f_z)$ is solved by the following equation:

$$\mathbf{B}(f_z) \mathbf{A}(f_z, \mathbb{S}_p) = \mathbf{A}(f_0, \mathbb{S}_p), \quad (4)$$

where \mathbb{S}_p is the set including all of the pre-estimated DoAs. Note that due to the unsolvability of the above equation in most cases, $\mathbf{B}(f_z)$ can be an approximate result rather than the exact one in practical. To obtain $\mathbf{B}(f_z)$ while balancing the exactness and the computational complexity, the RSS method is usually used, which realizes the following optimization [22]:

$$\arg \min_{\mathbf{B}(f_z)} [||\mathbf{A}(f_0, \mathbb{S}_p) - \mathbf{B}(f_z)\mathbf{A}(f_z, \mathbb{S}_p)||_F]. \quad (5)$$

The result of (5) is derived as [22]:

$$\mathbf{B}(f_z) = \mathbf{U}_R(f_z)\mathbf{U}_L^H(f_z), \quad (6)$$

where $\mathbf{U}_L(f_z)$ and $\mathbf{U}_R(f_z)$ denote the left and right singular matrix of $\mathbf{A}(f_z, \mathbb{S}_p)\mathbf{A}^H(f_0, \mathbb{S}_p)$ from singular value decomposition (SVD), respectively.

Then, CSM uses MUSIC algorithm to extract the information of DoAs and the signal source number \hat{N} from \mathbf{R}_Y [32]. Denote the noise-subspace matrix as \mathbf{E}_n . After forming \mathbf{E}_n with the eigenvectors of \mathbf{R}_Y in the noise-subspace, the MUSIC spatial spectrum is calculated as [7]:

$$\Theta_{\text{MUSIC}}(\theta, \phi) = \frac{1}{\mathbf{a}(f_0, \theta, \phi)\mathbf{E}_n\mathbf{E}_n^H\mathbf{a}^H(f_0, \theta, \phi)}, \quad (7)$$

where $\Theta_{\text{MUSIC}}(\theta, \phi)$ represents the entry of the spatial spectrum with elevation $\theta \in [0^\circ, 90^\circ]$ and azimuth $\phi \in [0^\circ, 360^\circ)$. The estimation results are identified as the first \hat{N} positions of peaks in the spatial spectrum by searching the spectrum with the elevation step v_θ and azimuth step v_ϕ . Therefore, $\Theta_{\text{MUSIC}}(\theta, \phi)$ is just calculated at the positions which are sampled from the range of spatial spectrum with v_θ and v_ϕ . To further improve the estimation performance, CSM can utilize these estimation results as the pre-estimated DoAs, and then update the estimation results iteratively [22].

Although CSM outperforms some classic DoA estimation methods, it suffers from the following two shortcomings. First, the errors between the pre-estimated DoAs and the actual ones significantly affect the DoA estimation performance [25], [26]. Second, the numerous frequency points, the spatial spectrum calculation and peak-searching process lead to high computational overhead.

III. THE PROPOSED METHOD

In this section, we first propose an efficient wideband 2D DoA estimation method named RIPF-CSM, and then its computational complexity is analysed and compared with the benchmark CSM methods.

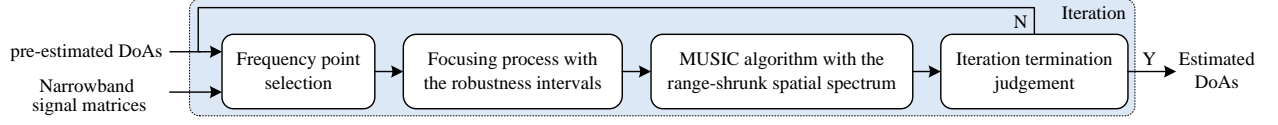


Fig. 2. The main structure of RIPF-CSM.

A. RIPF-CSM

In view of the above disadvantages of the conventional CSM, we propose RIPF-CSM which works in an iterative manner, and the maximum iteration number is I . Fig. 2 illustrates the main structure of RIPF-CSM. In this figure, the frequency point selection part randomly selects candidate frequency points for the subsequent focusing, the signal-subspaces at the candidate frequency points are focused into a reference frequency with the angles in the robustness intervals during the focusing process, the MUSIC algorithm estimates the DoA of the signals with range-shrunk spatial spectrum, and the last part judges whether the iteration should terminate. The details are described as follows.

1) Frequency point selection

We randomly select one frequency point to focus in the first iteration, and add this frequency point into the focusing frequency point set $\mathbb{F}_{\text{in}}^{(1)}$. In the i -th iterations ($i > 1$), $\mathbb{F}_{\text{in}}^{(i)}$ is generated by merging $\mathbb{F}_{\text{in}}^{(i-1)}$ and a certain number of other randomly selected frequency points. The number of frequency points added in each iteration affects DoA estimation performance and complexity, thus it should be elaborated. We define $\bar{\theta}_e$ and $\bar{\phi}_e$ as the average errors of elevation and azimuth of the pre-estimated DoAs, respectively. Denote $\bar{\delta}^{(i)}$ as the average difference between the estimated DoAs in the i -th iteration and those in the previous iteration, which is given as:

$$\bar{\delta}^{(i)} = \begin{cases} \frac{1}{2\hat{N}_i} \sum_{n=1}^{\hat{N}_i} |\hat{\theta}_n^{(i)} - \hat{\theta}_n^{(i-1)}| + |\hat{\phi}_n^{(i)} - \hat{\phi}_n^{(i-1)}|, & \text{if } \hat{N}_{i-1} = \hat{N}_i, \\ \frac{1}{2\hat{N}_i} \sum_{n=1}^{\hat{N}_i} \min \left[|\hat{\theta}_{n'}^{(i)} - \hat{\theta}_n^{(i-1)}| + |\hat{\phi}_{n'}^{(i)} - \hat{\phi}_n^{(i-1)}| \mid n' \in \{1, \dots, \hat{N}_{i-1}\} \right], & \text{if } \hat{N}_{i-1} \neq \hat{N}_i, \end{cases} \quad (8)$$

where \hat{N}_i , $\hat{\theta}_n^{(i)}$, $\hat{\phi}_n^{(i)}$ respectively denote the number of estimated DoAs, the estimated elevation and azimuth of the n -th signal source in the i -th iteration. Specially, \hat{N}_0 , $\hat{\theta}_n^{(0)}$, $\hat{\phi}_n^{(0)}$ denote the number of the pre-estimated DoAs, the elevation and azimuth of the n -th pre-estimated DoA, respectively. Based on the above definitions, the number of frequency points that are newly added into $\mathbb{F}_{\text{in}}^{(i)}$ in the i -th iteration is designed as:

$$\Delta_f^{(i)} = \min \left[\left\lceil \mu_f d_{\bar{\delta}}^{(i-1)} \right\rceil, Z - \left| \mathbb{F}_{\text{in}}^{(i-1)} \right| \right], \quad \text{if } i > 1, \quad (9)$$

where $\mu_f = Z/I + (d_\theta + d_\phi)/2$ is a constant, $d_\theta = \bar{\theta}_e/1^\circ$, $d_\phi = \bar{\phi}_e/1^\circ$, and $d_{\bar{\delta}}^{(i-1)} = \bar{\delta}^{(i-1)}/1^\circ$. The second term of $\min[\cdot]$ in (9) is set to prevent $|\mathbb{F}_{\text{in}}^{(i)}|$ exceeding Z . Considering the focusing performance may vary at different frequency points, we discuss the first term of $\min[\cdot]$ in (9). First, $\Delta_f^{(i)}$ is set to be positively related with μ_f and thus Z/I to improve the reliability. Such setting guarantees $|\mathbb{F}_{\text{in}}^{(i)}|$ increases with the increase of Z , and also ensures the amount of candidate frequency points even if I is small. Second, to avoid the phenomenon that the estimation converges with unsatisfactory focusing performance, $\lceil \cdot \rceil$ in (9) sets a lower bound for $\mu_f d_{\bar{\delta}}^{(i-1)}$ to 1 in order to keep $\mathbb{F}_{\text{in}}^{(i)}$ updating. Thus, it is possible for the results in the next iteration to be refined by the information from at least one newly added frequency point before the convergence. Third, $\Delta_f^{(i)}$ grows with the increase of μ_f and thus d_θ and d_ϕ to remedy unsatisfactory pre-estimated DoAs which can invoke the unfavorable phenomenon that the focused manifold matrices deviate greatly from the exact ones. Furthermore, as shown in (8), since $\bar{\delta}^{(i)}$ reflects the corresponding convergence degree of the i -th iteration results ($i > 1$), $\Delta_f^{(i)}$ is positively related with $\bar{\delta}^{(i-1)}$ so as to reduce unnecessary complexity while maintaining the DoA estimation performance. Set $\Delta_f^{(1)} = 0$ for simplicity, and then the number of candidate frequency points in the i -th iteration is given as:

$$Z_{\text{in}}^{(i)} = 1 + \sum_{i'=1}^i \Delta_f^{(i')}, \quad (10)$$

2) Focusing process with the robustness intervals

In this part, the narrowband signal matrices at the candidate frequency points are dealt with. The focusing angles of the focusing process are sampled from our designed angle intervals which are called robustness intervals. In the i -th iteration, the centers of the robustness intervals are set to be $(\hat{\theta}_n^{(i-1)}, \hat{\phi}_n^{(i-1)})$ where $n = 1, 2, \dots, \hat{N}_{i-1}$, and the robustness interval radii of elevation and azimuth are respectively denoted as $R_n^\theta(i)$ and $R_n^\phi(i)$. Based on the centers and radii, the robustness intervals are given as:

$$\mathbb{G}_n^\theta(i) = [\max[0^\circ, \hat{\theta}_n^{(i-1)} - R_n^\theta(i)], \min[\hat{\theta}_n^{(i-1)} + R_n^\theta(i), 90^\circ]], \quad (11)$$

$$\mathbb{G}_n^\phi(i) = [\hat{\phi}_n^{(i-1)} - R_n^\phi(i), \hat{\phi}_n^{(i-1)} + R_n^\phi(i)], \quad (12)$$

where $\mathbb{G}_n^\theta(i)$ and $\mathbb{G}_n^\phi(i)$ respectively denote the n -th robustness intervals of elevation and azimuth, and the part of $\mathbb{G}_n^\phi(i)$ that exceeds $[0^\circ, 360^\circ)$ is converted to the corresponding range in $[0^\circ, 360^\circ)$ based on the periodicity of azimuth. Then, we obtain the focusing angles by sampling the range

constrained by $\mathbb{G}_n^\theta(i)$ and $\mathbb{G}_n^\phi(i)$, $n=1,2,\dots,\hat{N}_{i-1}$, with the elevation step v_θ and azimuth step v_ϕ .

The robustness interval radii $R_n^\theta(i)$ and $R_n^\phi(i)$ in (11) and (12) are designed as follows. Since the focusing angles close to the actual DoAs improve the focusing performance and the focusing angles that are far away from the actual DoAs cause performance loss [22], focusing angles should be as close to the actual DoAs as possible while maintaining concise. To achieve such purpose, we design $R_n^\theta(i)$ and $R_n^\phi(i)$ as:

$$R_n^\theta(i) = \frac{\bar{\theta}_e [b - \cos \hat{\theta}_n^{(i-1)}] d_{\bar{\delta}}^{(i-1)}}{i}, \quad (13)$$

$$R_n^\phi(i) = \frac{\bar{\phi}_e [b - \sin \hat{\theta}_n^{(i-1)}] d_{\bar{\delta}}^{(i-1)}}{i} \quad (14)$$

where $R_n^\theta(i)$ and $R_n^\phi(i)$ respectively stand for the n -th robustness interval radii of elevation and azimuth in the i -th iteration, $n \in \{1, 2, \dots, \hat{N}_i\}$, $b > 1$ denotes an adjustable bias, and $d_{\bar{\delta}}^{(0)}$ is set to be 1 as a coefficient without effects on the radii in the first iteration. In (13) and (14), $R_n^\theta(i)$ and $R_n^\phi(i)$ are positively related with $\bar{\theta}_e$ and $\bar{\phi}_e$ respectively, so that the range constrained by robustness intervals can generally cover the actual DoAs and thus achieve the robustness to the errors of pre-estimated DoAs. Since the estimation results become more and more accurate with iterations, $R_n^\theta(i)$ and $R_n^\phi(i)$ are designed to be negative to i as shown in (13) and (14) to decrease the number of the focusing angles which are far from actual DoAs, thereby further improving the performance and reducing computational complexity. $\bar{\delta}^{(i)}$ in (8) reflects the estimation accuracy of the i -th iteration ($i > 1$), so $R_n^\theta(i)$ and $R_n^\phi(i)$ in (13) and (14) decrease when $\bar{\delta}^{(i-1)}$ becomes smaller to improve accuracy and reduce computational overhead. Furthermore, the design of $R_n^\theta(i)$ and $R_n^\phi(i)$ should consider the steering vectors of adjacent angles. Specifically, if the absolute values of the partial derivatives of $\mathbf{a}(f_z, \theta_n, \phi_n)$ are small, the adjacent angles are easily to be confused if the noise is present, which affects the DoA estimation accuracy. For this issue, we first give the partial derivatives $\boldsymbol{\rho}_z^n(\tau) = \partial \mathbf{a}(f_z, \theta_n, \phi_n) / \partial \tau$ with $\tau \in \{\theta_n, \phi_n\}$ as:

$$\boldsymbol{\rho}_z^n(\theta_n) = j \frac{2\pi r f_z}{c} \cos \theta_n \times \text{diag} \left[\cos(-\phi_n), \dots, \cos \left(\frac{2\pi \times (M-1)}{M} - \phi_n \right) \right] \mathbf{a}(f_z, \theta_n, \phi_n), \quad (15)$$

$$\boldsymbol{\rho}_z^n(\phi_n) = j \frac{2\pi r f_z}{c} \sin \theta_n \times \text{diag} \left[\sin(-\phi_n), \dots, \sin \left(\frac{2\pi \times (M-1)}{M} - \phi_n \right) \right] \mathbf{a}(f_z, \theta_n, \phi_n). \quad (16)$$

Then, $R_n^\theta(i)$ and $R_n^\phi(i)$ are respectively designed to be negatively related with $\cos \hat{\theta}_n^{(i-1)}$ and $\sin \hat{\theta}_n^{(i-1)}$ and thus the partial derivatives. In such way, the radii are adaptively adjusted to enable the improved discrimination of adjacent angles. In addition, the bias b in (13) and (14) is used to control the sensitivity of the radii to the partial derivatives. By adjusting the value of b , the

degree of influence of $\cos \hat{\theta}_n^{(i-1)}$ and $\sin \hat{\theta}_n^{(i-1)}$ on $R_n^\theta(i)$ and $R_n^\phi(i)$ can be respectively changed, thereby affecting the sensitivity.

Define the set of focusing angles in the i -th iteration as \mathbb{S}_p^i . The focusing matrices at the frequency points in $\mathbb{F}_{\text{in}}^{(i)}$ are calculated by (6) where the source matrix of SVD is replaced by $\mathbf{A}(f_z, \mathbb{S}_p^i) \mathbf{A}^H(f_0, \mathbb{S}_p^i)$. Then \mathbf{R}_Y is computed as:

$$\mathbf{R}_Y = \frac{1}{K_f Z^2} \sum_{z \in \mathbb{F}_{\text{in}}^{(i)}} [\mathbf{B}(f_z) \mathbf{X}_f(f_z)] [\mathbf{B}(f_z) \mathbf{X}_f(f_z)]^H. \quad (17)$$

3) MUSIC algorithm with the range-shrunk spatial spectrum

Based on the derived DoAs in the i -th iteration, i.e., $(\hat{\theta}_n^{(i-1)}, \hat{\phi}_n^{(i-1)})$ where $n = 1, 2, \dots, \hat{N}_{i-1}$, it is unnecessary to generate the whole spatial spectrum of MUSIC algorithm as mentioned in Section II-B, since actual DoAs are generally not far from the pre-estimated DoAs [21]–[26] as well as $(\hat{\theta}_n^{(i-1)}, \hat{\phi}_n^{(i-1)})$. To reduce the computational burden, we shrink the range of spatial spectrum to the regions constrained by $\mathbb{G}_n^\theta(i)$ and $\mathbb{G}_n^\phi(i)$, $n = 1, 2, \dots, \hat{N}_{i-1}$, since these regions are designed to cover the actual DoAs in most cases as mentioned in the previous part. Afterwards, the MUSIC algorithm with the range-shrunk spatial spectrum is utilized to estimate the DoAs based on \mathbf{R}_Y in (17).

4) Iteration termination judgement

In each iteration, the estimation results are sent to the iteration termination judgement part. The iteration terminates when either the estimation results are equal to the ones that are derived in the previous iteration, or the number of iterations reaches the maximum number I . The results of the last iteration are the eventual estimated DoAs.

To sum up, by extending the conventional CSM, our proposed method improves the robustness of focusing process by generating the focusing angles from the robustness intervals in Part 2), and the computational complexity is reduced by considering less frequency points in Part 1) and shrinking the range of the spatial spectrum in Part 3). When RSS method is chosen to generate the focusing matrices, the procedure of RIPF-CSM is summarized in Algorithm 1.

B. Analysis and Comparison of Computational Complexity

In this paper, the number of floating-point operations (FLOPs) is used to represent the computational complexity. We first discuss the computational complexity of RIPF-CSM with RSS method in a single iteration. The complexity of arithmetic operations and logic judgements in Algorithm 1 is easy to count, and thus we focus on the other operations, including trigonometric

Algorithm 1 RIPF-CSM with RSS method.

Input: $M, r, b, f_0, Z, I, \bar{\theta}_e, \bar{\phi}_e, v_\theta, v_\phi, \mathbf{X}_f(f_1), \dots, \mathbf{X}_f(f_Z), f_1, \dots, f_Z, (\hat{\theta}_1^{(0)}, \hat{\phi}_1^{(0)}), \dots, (\hat{\theta}_{\hat{N}_0}^{(0)}, \hat{\phi}_{\hat{N}_0}^{(0)})$.

Output: Estimated DoAs of the wideband signal sources.

1: **Initialization:** Compute μ_f, d_θ, d_ϕ , and set i as 1.

2: **while** $i \leq I$ **do**

Frequency point selection:

3: **if** $i = 1$ **then**

4: Select a frequency point randomly and form $\mathbb{F}_{\text{in}}^{(1)}$.

5: **else**

6: Calculate $\Delta_f^{(i)}$ by (9), randomly select $\Delta_f^{(i)}$ frequency points which are not in $\mathbb{F}_{\text{in}}^{(i-1)}$ and merge them with $\mathbb{F}_{\text{in}}^{(i-1)}$ to form $\mathbb{F}_{\text{in}}^{(i)}$.

7: **end if**

Focusing process:

8: Calculate $R_n^\theta(i)$ and $R_n^\phi(i)$ by (13) and (14). Generate $\mathbb{G}_n^\theta(i)$ and $\mathbb{G}_n^\phi(i)$ by (11) and (12).

9: Form \mathbb{S}_p^i by sampling $\mathbb{G}_n^\theta(i)$ and $\mathbb{G}_n^\phi(i)$ with v_θ and v_ϕ .

10: Compute $\mathbf{A}(f_z, \mathbb{S}_p^i) \mathbf{A}^H(f_0, \mathbb{S}_p^i)$ at all $f_z \in \mathbb{F}_{\text{in}}^{(i)}$, and then calculate the corresponding $\mathbf{B}(f_z)$ by substituting the SVD results of $\mathbf{A}(f_z, \mathbb{S}_p^i) \mathbf{A}^H(f_0, \mathbb{S}_p^i)$ into (6).

11: Compute \mathbf{R}_Y by (17).

MUSIC algorithm:

12: Perform EVD on \mathbf{R}_Y , and identify \hat{N}_i in (8) by the difference between the eigenvalues.

13: Form \mathbf{E}_n by the eigenvectors of the noise-subspace.

14: Sample the range constrained by $\mathbb{G}_n^\theta(i)$ and $\mathbb{G}_n^\phi(i)$, $n = 1, 2, \dots, \hat{N}_{i-1}$, with the steps v_θ and v_ϕ , and then compute the spatial spectrum at sampled positions by (7).

15: Estimate $(\hat{\theta}_1^{(i)}, \hat{\phi}_1^{(i)}), \dots, (\hat{\theta}_{\hat{N}_i}^{(i)}, \hat{\phi}_{\hat{N}_i}^{(i)})$ by searching for the largest \hat{N}_i spatial spectrum peaks.

Iteration termination judgement:

16: Calculate $\bar{\delta}^{(i)}$ by (8).

17: **if** $\bar{\delta}^{(i)} = 0$ **and** $\hat{N}_{i-1} = \hat{N}_i$ **then**

18: **exit while**

19: **end if**

20: Compute $d_{\bar{\delta}}^{(i)}$ in (9), and update i by $i + 1$.

21: **end while**

22: **return** $(\hat{\theta}_1^{(i)}, \hat{\phi}_1^{(i)}), (\hat{\theta}_2^{(i)}, \hat{\phi}_2^{(i)}), \dots, (\hat{\theta}_{\hat{N}_i}^{(i)}, \hat{\phi}_{\hat{N}_i}^{(i)})$

functions, SVD and EVD. The computational complexity of trigonometric function is regarded as a small and constant amount of FLOPs which varies at the demands of different precisions [33]. In addition, the computational complexity of SVD is generally twice as much as that of EVD [34] whose complexity is expressed as $\mathcal{O}(M^3)$ FLOPs [35]. Based on the above arguments and the details in Algorithm 1, the total computational complexity of the RIPF-CSM with RSS method is calculated as $\mathcal{O}(2Z_{\text{in}}^{(i)} M^2 [M + 8K_f + 16 \sum_{n=1}^{\hat{N}_{i-1}} R_n^\theta(i) R_n^\phi(i) / (v_\theta v_\phi)])$ by summarizing the complexity of all operations and just keeping the highest order terms of the parameters in the complexity expression.

To better reveal the complexity advantage of the proposed method, we also count the computational complexity of the benchmark CSM methods, i.e., conventional CSM (C-CSM), conventional CSM with specific extra focusing angles (SE-CSM) [22], R-CSM [25] and I-2D-CSM [26]. For fair comparison, all of their acquisition processes of the pre-estimated DoAs are not taken into account in this paper, and these methods for 1D DoA estimation are first extended to the corresponding version for 2D DoA estimation as shown in Appendix A. Considering the focusing matrices of the methods for comparison are generated by RSS method, there are three differences in terms of complexity between the proposed method and other methods. First, the methods for comparison use all the Z frequency points rather than partial frequency points. Second, there exists differences in the number of focusing angles between RIPF-CSM and other benchmark methods, which are controlled by the radii of robustness intervals. The radii of robustness intervals of C-CSM and SE-CSM are respectively equivalent to 0 and 1. Additionally, the elevation and azimuth robustness interval radii of R-CSM are respectively defined as $R_n^{\theta'}(i)$ and $R_n^{\phi'}(i)$, and those of I-2D-CSM are respectively defined as $R_n^{\theta''}(i)$ and $R_n^{\phi''}(i)$, which are given in Appendix A. Third, the range of the spatial spectrum in the benchmark methods is constrained by $\theta \in [0^\circ, 90^\circ]$ and $\phi \in [0^\circ, 360^\circ)$ rather than robustness intervals. The numbers of elevation and azimuth angles sampled within the aforementioned range are respectively denoted as $L_\theta = 90^\circ / v_\theta + 1$ and $L_\phi = 360^\circ / v_\phi$. According to the above discussions, the computational complexity of each method in a single iteration is summarized in TABLE I.

It is observed from TABLE I that there is only one different term in the complexity expressions of the first four methods. Since v_θ and v_ϕ are usually not greater than 1° [7], [14], [15] and R-CSM requires about five iterations to converge [25], $R_n^{\theta'}(i) R_n^{\phi'}(i) / (v_\theta v_\phi) > 1/4$ holds. Moreover, according to Appendix A and $v_\theta, v_\phi \leq 1^\circ$, we have $i_s^\theta, i_s^\phi \leq 2$, then $R_n^{\theta''}(i) R_n^{\phi''}(i) / (v_\theta v_\phi) > 1/4$

TABLE I
COMPUTATIONAL COMPLEXITY OF DIFFERENT CSM METHODS

Method	Complexity in a single iteration / FLOPs
C-CSM	$\mathcal{O}\left(2\mathbf{Z}M^2(M + 8K_f + 4\hat{N}_{i-1}) + 8M^2\mathbf{L}_\theta\mathbf{L}_\phi\right)$
SE-CSM	$\mathcal{O}\left(2\mathbf{Z}M^2(M + 8K_f + 20\hat{N}_{i-1}) + 8M^2\mathbf{L}_\theta\mathbf{L}_\phi\right)$
R-CSM	$\mathcal{O}\left(2\mathbf{Z}M^2[M + 8K_f + 16 \sum_{n=1}^{\hat{N}_{i-1}} \mathbf{R}_n^{\theta'}(i)\mathbf{R}_n^{\phi'}(i)/(v_\theta v_\phi)] + 8M^2\mathbf{L}_\theta\mathbf{L}_\phi\right)$
I-2D-CSM	$\mathcal{O}\left(2\mathbf{Z}M^2[M + 8K_f + 16 \sum_{n=1}^{\hat{N}_{i-1}} \mathbf{R}_n^{\theta''}(i)\mathbf{R}_n^{\phi''}(i)/(v_\theta v_\phi)] + 8M^2\mathbf{L}_\theta\mathbf{L}_\phi\right)$
RIPF-CSM	$\mathcal{O}\left(2\mathbf{Z}_{\text{in}}^{(i)}M^2[M + 8K_f + 16 \sum_{n=1}^{\hat{N}_{i-1}} \mathbf{R}_n^\theta(i)\mathbf{R}_n^\phi(i)/(v_\theta v_\phi)]\right)$

holds for I-2D-CSM. Based on these inequalities, the computational complexity of C-CSM is lower than that of SE-CSM, R-CSM and I-2D-CSM in a single iteration. To guarantee the complexity advantage of RIPF-CSM in a single iteration when compared with C-CSM, there exists one parameter constraint such that $Z_{\text{in}}^{(i)} \left[M + 8K_f + 16 \sum_{n=1}^{\hat{N}_i} R_n^\theta(i)R_n^\phi(i)/(v_\theta v_\phi) \right] < Z(M + 4\hat{N}_i + 8K_f) + 4L_\theta L_\phi$, which can be easily satisfied and is discussed in Appendix B. Verified by the simulations with general parameters in practical scenarios, the number of iterations of the proposed method is significantly less than that of C-CSM and SE-CSM, and approximately equal to that of R-CSM and I-2D-CSM. Thus, based on the complexity in a single iteration and the number of iterations as discussed above, RIPF-CSM enjoys lower overall computational complexity when compared with the existing benchmarks.

IV. CRAMÉR-RAO BOUND

In this section, we first develop the CRB of the scenario considered in this paper, i.e., 2D DoA estimation with UCA for multiple wideband signal sources with multiple snapshots. Then, the guidelines for practical applications are discussed based on the derived CRB expression.

A. Derivation of CRB

We denote the k -th snapshot vectors in frequency domain of $\mathbf{X}_f(f_z)$, $\mathbf{S}_f(f_z)$ and $\mathbf{W}_f(f_z)$ as $\mathbf{x}_f(k, f_z) \in \mathbb{C}^{M \times 1}$, $\mathbf{s}_f(k, f_z) \in \mathbb{C}^{N \times 1}$ and $\mathbf{w}(k, f_z) \in \mathbb{C}^{M \times 1}$ respectively, where $k \in \{1, 2, \dots, K_f\}$ and $z \in \{1, 2, \dots, Z\}$. These vectors satisfy the following equation:

$$\mathbf{x}_f(k, f_z) = \mathbf{A}(f_z, \mathbb{S})\mathbf{s}_f(k, f_z) + \mathbf{w}(k, f_z). \quad (18)$$

where $\mathbf{d}_\zeta = \partial \ln P / \partial \zeta$. We define the $2N$ -order square matrix in the lower right corner of \mathbf{F}^{-1} as $\mathbf{F}_{\text{inv}}(\zeta)$. Based on the formula for the inverse of block matrix, $\mathbf{F}_{\text{inv}}(\zeta)$ is calculated as:

$$\mathbf{F}_{\text{inv}}(\zeta) = \frac{Z\sigma^2}{2} \left[\sum_{k=1}^{K_f} \sum_{z=1}^Z \text{Re} [\boldsymbol{\Xi}^H(k, f_z) \mathbf{D}^H(f_z) \mathbf{P}_A^\perp(f_z) \mathbf{D}(f_z) \boldsymbol{\Xi}(k, f_z)] \right]^{-1}, \quad (29)$$

where $\mathbf{P}_A^\perp(f_z) = \mathbf{I}_M - \mathbf{P}_A(f_z) = \mathbf{I}_M - \mathbf{A}(f_z) [\mathbf{A}^H(f_z) \mathbf{A}(f_z)]^{-1} \mathbf{A}^H(f_z)$ and $\mathbf{P}_A(f_z)$ is an orthogonal projection matrix. According to the definition of CRB in [12], the main diagonal elements of $\mathbf{F}_{\text{inv}}(\zeta)$ are the CRBs of $\theta_1, \dots, \theta_N, \phi_1, \dots, \phi_N$, respectively.

B. Discussions

It is well-known that a smaller CRB corresponds to an improved accuracy of parameter estimation. Based on this fact, we give some discussions on the terms that affect the CRB.

- **The sampling duration:** As shown in (29), the larger K_f is, the smaller CRBs of DoAs are. Thus, the DoA estimation performance can be improved by increasing the sampling duration t_0 when the sampling rate f_s remains unchanged.
- **The channel bandwidth:** According to the Nyquist sampling theorem, wider signal bandwidth requires higher sampling rate, which implies an increased K_f when t_0 remains unchanged, thereby decreasing the CRB.
- **The signal power:** (29) can be rewritten as:

$$\mathbf{F}_{\text{inv}}(\zeta) = \frac{Z\sigma^2}{2} \left[\sum_{k=1}^{K_f} \sum_{z=1}^Z \text{Re} [(\mathbf{D}^H(f_z) \mathbf{P}_A^\perp(f_z) \mathbf{D}(f_z)) \odot \mathbf{R}_{2S}(k, f_z)] \right]^{-1}, \quad (30)$$

where $\mathbf{R}_{2S}(k, f_z) = \boldsymbol{\Xi}^H(k, f_z) \mathbf{1}_{2N} \boldsymbol{\Xi}(k, f_z)$. It is easy to know that the increase of the signal power enlarges the magnitude of the elements in $\mathbf{R}_{2S}(k, f_z)$ and thus the CRB decreases.

- **The number of array elements:** $\mathbf{D}^H(f_z) \mathbf{P}_A^\perp(f_z) \mathbf{D}(f_z)$ in (29) can be expanded as:

$$\mathbf{D}^H(f_z) \mathbf{P}_A^\perp(f_z) \mathbf{D}(f_z) = \mathbf{D}^H(f_z) \mathbf{D}(f_z) - \mathbf{D}^H(f_z) \mathbf{P}_A(f_z) \mathbf{D}(f_z), \quad (31)$$

where the element in the q_1 -th row and q_2 -th column of $\mathbf{D}^H(f_z) \mathbf{D}(f_z)$ can be written as:

$$[\mathbf{D}^H(f_z) \mathbf{D}(f_z)]_{q_1 q_2} = \begin{cases} (2\pi r f_z / c)^2 \text{Pe}_1(r, f_z, \theta_{q_1}, \theta_{q_2}), & \text{if } q_1 \leq N, q_2 \leq N, \\ (2\pi r f_z / c)^2 \text{Pe}_2(r, f_z, \theta_{q_1}, \phi_{q_2-N}), & \text{if } q_1 \leq N, q_2 > N, \\ (2\pi r f_z / c)^2 \text{Pe}_3(r, f_z, \phi_{q_1-N}, \theta_{q_2}), & \text{if } q_1 > N, q_2 \leq N, \\ (2\pi r f_z / c)^2 \text{Pe}_4(r, f_z, \phi_{q_1-N}, \phi_{q_2-N}), & \text{if } q_1 > N, q_2 > N, \end{cases} \quad (32)$$

where $q_1, q_2 \in \{1, \dots, 2N\}$ and $\text{Pe}_q(r, f_z, \tau_1, \tau_2)$ represents a periodic function that is the product of multiple periodic functions according to (15) and (16), $\tau_1, \tau_2 \in \{\theta_1, \dots, \theta_N, \phi_1, \dots, \phi_N\}$, $q \in \{1, 2, 3, 4\}$, and its period is related with r, f_z, τ_1, τ_2 . Due to the periodicity of $\text{Pe}_q(r, f_z, \tau_1, \tau_2)$, we ignore its effect on the magnitude of $[\mathbf{D}^H(f_z)\mathbf{D}(f_z)]_{q_1q_2}$. As a result, the detailed expressions are omitted for conciseness. Considering the coefficient $(2\pi r f_z/c)^2$ in (32), the magnitude of each element in $\mathbf{D}^H(f_z)\mathbf{D}(f_z)$ is positively related with the radius r of UCA which grows as the number M of array elements increases. Since $\mathbf{P}_A(f_z)$ is an idempotent Hermitian matrix, $\mathbf{D}^H(f_z)\mathbf{P}_A(f_z)\mathbf{D}(f_z)$ can be expanded as:

$$\mathbf{D}^H(f_z)\mathbf{P}_A(f_z)\mathbf{D}(f_z) = [\mathbf{P}_A(f_z)\mathbf{D}(f_z)]^H[\mathbf{P}_A(f_z)\mathbf{D}(f_z)], \quad (33)$$

where $\mathbf{P}_A(f_z)\mathbf{D}(f_z)$ is equivalent to projecting $\mathbf{D}(f_z)$ into a low-dimensional subspace. Accordingly, the result of (33) is similar to $\mathbf{D}^H(f_z)\mathbf{D}(f_z)$, i.e., each element in the result of (33) is the product of the coefficient $(2\pi r f_z/c)^2$ and a certain periodic function like (32). Thus, the number of array elements is generally negative to the CRB.

According to the above arguments and (30), the CRBs, i.e., the main diagonal elements of $\mathbf{F}_{\text{inv}}(\zeta)$, are generally inversely proportional to K_f, r and thus $1/\sin(\pi/M)$, and the magnitude of the elements in $\mathbf{R}_{2S}(k, f_z)$. Note that the derivatives of $1/K_f, \sin(\pi/M)$ and $1/P_S$ with respect to their respective variables are $-1/K_f^2, -\cos(\pi/M)/M^2$ and $-1/P_S^2$ where P_S represents the average power of the signals. Therefore, by adopting the strategy that increases the corresponding variables of the above derivatives especially the smallest derivative, which includes the number of snapshots (equivalent to the sampling duration or the channel bandwidth), the signal power and the number of array elements, the accuracy of wideband 2D DoA estimation with UCA can be improved effectively.

V. SIMULATION RESULTS AND ANALYSIS

In this section, we provide the numerical simulation results of our proposed RIPF-CSM method. Its performance and computational complexity are compared with the aforementioned benchmark methods, i.e., C-CSM with a single iteration (C-CSM ($i = 1$)), C-CSM, SE-CSM, R-CSM and I-2D-CSM.

Root mean square error (RMSE) and successful detection probability (SDP) [36]–[38] are used as metrics to measure the DoA estimation performance. Among them, RMSE indicates the degree of the deviation between the estimation results and the actual DoAs, which is defined as:

$$\text{RMSE} = \sqrt{\frac{\sum_{\kappa=1}^{\mathcal{M}} \sum_{n=1}^N (\hat{\theta}_n(\kappa) - \theta_n)^2 + (\hat{\phi}_n(\kappa) - \phi_n)^2}{\mathcal{M}N}}, \quad (34)$$

where \mathcal{M} is the number of Monte Carlo experiments, $\hat{\theta}_n(\kappa)$ and $\hat{\phi}_n(\kappa)$ respectively denote the elevation and azimuth of the n -th estimated DoA in the κ -th experiment. Additionally, the RMSE corresponding to the average CRB of different DoAs is calculated as:

$$\text{RMSE}_{\text{CRB}} = \sqrt{\frac{\sum_{v=1}^V \text{trace}[\mathbf{F}_{\text{inv}}(\boldsymbol{\zeta}_v)]}{VN}}, \quad (35)$$

where we define the DoAs considered simultaneously as a DoA group, V represents the number of DoA groups and $\boldsymbol{\zeta}_v$ stands for $\boldsymbol{\zeta}$ in (29) of the v -th group. SDP is the probability that the 2D DoA estimation results are close to the actual ones, which is used to reflect the validity of DoA estimation directly. It is defined as:

$$\text{SDP} = \mathcal{P} \left(\left| \hat{\theta}_n - \theta_n \right| + \left| \hat{\phi}_n - \phi_n \right| \leq v_\theta + v_\phi \right). \quad (36)$$

In addition, we use running time to represent the computational complexity. The simulation platform is MatlabR2020a on a computer with 2.10GHz AMD Ryzen 5-4600U CPU and 16GB random access memory.

A. Simulation Settings

In the simulations, the number M of UCA antenna elements is set as 5. The speed of light $c = 3 \times 10^8 \text{m/s}$. The received signals are linear frequency modulated signals with $f_0 = 30 \text{GHz}$, which are converted to analytic signals. The bandwidth B of them and the sampling rate f_s are respectively set as 9GHz and 11.25GHz, and the sampling duration is $t_0 = 10 \mu\text{s}$. Besides, the radius of UCA is set as $r = c / (4(f_0 + B/2) \sin(\pi/M))$. We consider the scenario with approximately coherent signals, i.e., the same signal arrives at the antenna array from different paths successively, and the DoA estimation of which is more difficult than that with uncorrelated signals. The time intervals between adjacent arriving paths are set to be 1ns to generate approximately coherent signals, thereby revealing the universal applicability of RIPF-CSM. To display the performance and computational complexity of each method under different numbers of paths, we give the results when $N = 1, 2, 3$, respectively. In addition, for each case of path number, we respectively select three different DoA groups as shown in TABLE II. The

TABLE II
GROUND-TRUTH DOAs IN DIFFERENT GROUPS

N	Group	DoA
1	1	$(60^\circ, 150^\circ)$
	2	$(33^\circ, 50^\circ)$
	3	$(28^\circ, 230^\circ)$
2	1	$(60^\circ, 150^\circ), (20^\circ, 45^\circ)$
	2	$(40^\circ, 175^\circ), (70^\circ, 250^\circ)$
	3	$(25^\circ, 230^\circ), (65^\circ, 150^\circ)$
3	1	$(60^\circ, 150^\circ), (30^\circ, 95^\circ), (45^\circ, 300^\circ)$
	2	$(30^\circ, 50^\circ), (40^\circ, 190^\circ), (70^\circ, 250^\circ)$
	3	$(25^\circ, 230^\circ), (65^\circ, 150^\circ), (35^\circ, 60^\circ)$

simulation results of different groups with same N are counted together.

Furthermore, the performance and the computational complexity are given for different SNR, $\bar{\theta}_e$, $\bar{\phi}_e$, Z , v_θ and v_ϕ , and the default values of these parameters are SNR = 10dB, $\bar{\theta}_e = \bar{\phi}_e = 3^\circ$, $Z = 32$ and $v_\theta = v_\phi = 0.2^\circ$. We keep $Z \geq 32$ to guarantee the bandwidth corresponding to each frequency point is far less than the central frequency f_0 , which can be considered as narrowband. Moreover, we set $b = 3$ and $I = 15$. Each simulation result is obtained by performing $\mathcal{M} = 200$ Monte Carlo experiments.

B. RMSE and SDP Versus SNR

When SNR varies and $N = 1, 2, 3$, this subsection gives the RMSE and SDP of different methods as shown in Fig. 3. We also depict the RMSE of average CRB as a benchmark.

As illustrated in Fig. 3, for any SNR in the simulations, the RMSE and the SDP of RIPF-CSM are both better than those of other methods. Moreover, although the estimation accuracy of all the methods becomes worse with a larger N , RIPF-CSM is always optimal. Since the difference of the performance between the proposed method and the benchmark methods is mainly affected by the focusing process, it implies that the focusing process with the robustness intervals of RIPF-CSM generates more effective focusing matrices, thereby significantly improving the DoA estimation performance.

In addition, it is observed from Fig. 3 that when SNR increases, the RMSE of our proposed method decreases, and the SDP of it increases. Furthermore, Fig. 3 also shows that RIPF-CSM requires lower SNR to achieve the same estimation performance as that of the benchmark methods, which indicates the favorable robustness of RIPF-CSM. Besides, RIPF-CSM can achieve

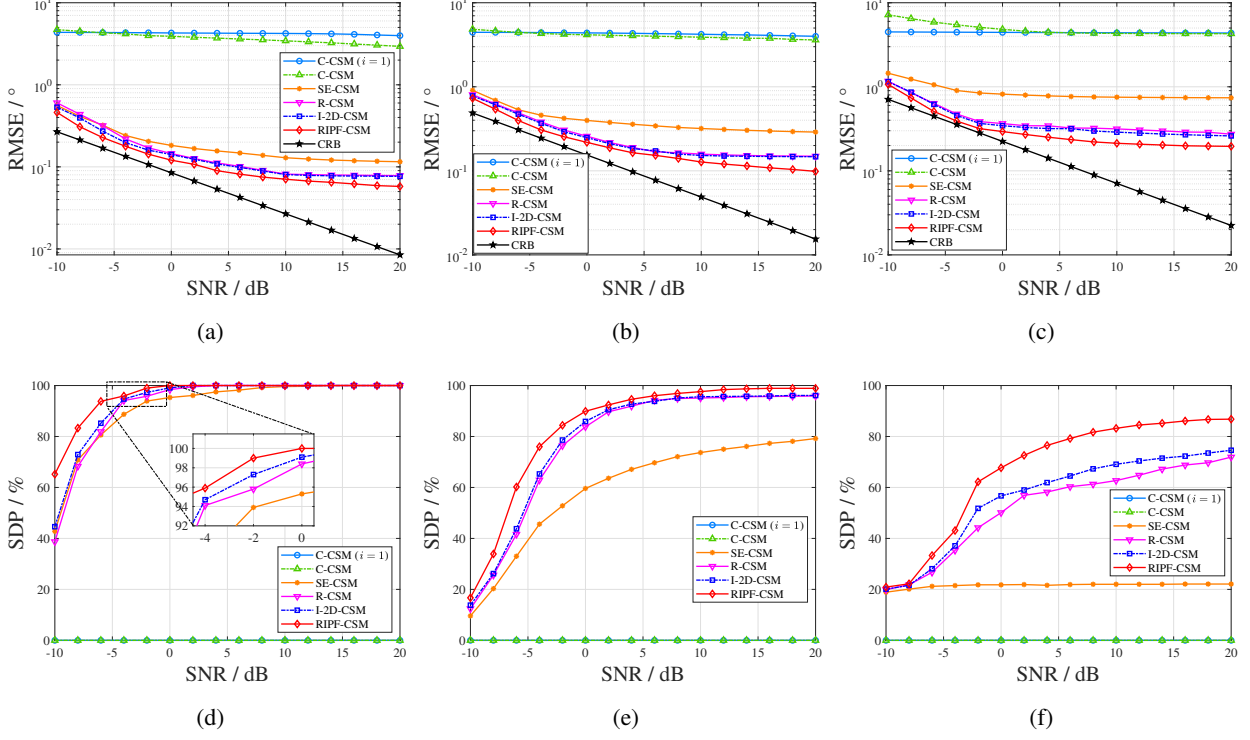


Fig. 3. RMSE and SDP of estimation results in $\text{SNR} \in [-10\text{dB}, 20\text{dB}]$. (a) and (d) are with $N = 1$; (b) and (e) are with $N = 2$; (c) and (f) are with $N = 3$.

excellent performance which is fairly close to CRB when $\text{SNR} \in [-2\text{dB}, -6\text{dB}]$ as shown in Figs. 3 (a)-(c).

C. RMSE and Running Time Versus the Average Errors of Pre-estimated DoAs

Compared with SDP, RMSE can better reflect the errors of estimation results according to (34) and (36). Thus, we choose RMSE to evaluate the accuracy of the proposed method in this subsection. When $\bar{\theta}_e$ and $\bar{\phi}_e$ vary and $N = 1, 2, 3$, this subsection gives the RMSE and running time of different methods as shown in Fig. 4. The RMSE of average CRB is also depicted.

It can be observed from Figs. 4 (a)-(c) that for any $\bar{\theta}_e$, $\bar{\phi}_e$ and N in the simulations, RIPP-CSM exhibits better performance when compared with the benchmark methods and its RMSE is closer to CRB with the decrease of $\bar{\theta}_e$ and $\bar{\phi}_e$, which demonstrates that the proposed robustness intervals can make full use of the pre-estimated DoAs and reveals the robustness of RIPP-CSM to different errors of pre-estimated DoAs. In contrast, Figs. 4 (a)-(c) show that the RMSE of SE-CSM, R-CSM and I-2D-CSM almost keep still for any $\bar{\theta}_e$ and $\bar{\phi}_e$. It is due to the reason that most of their focusing angles are far from actual DoAs, which makes the focusing process be

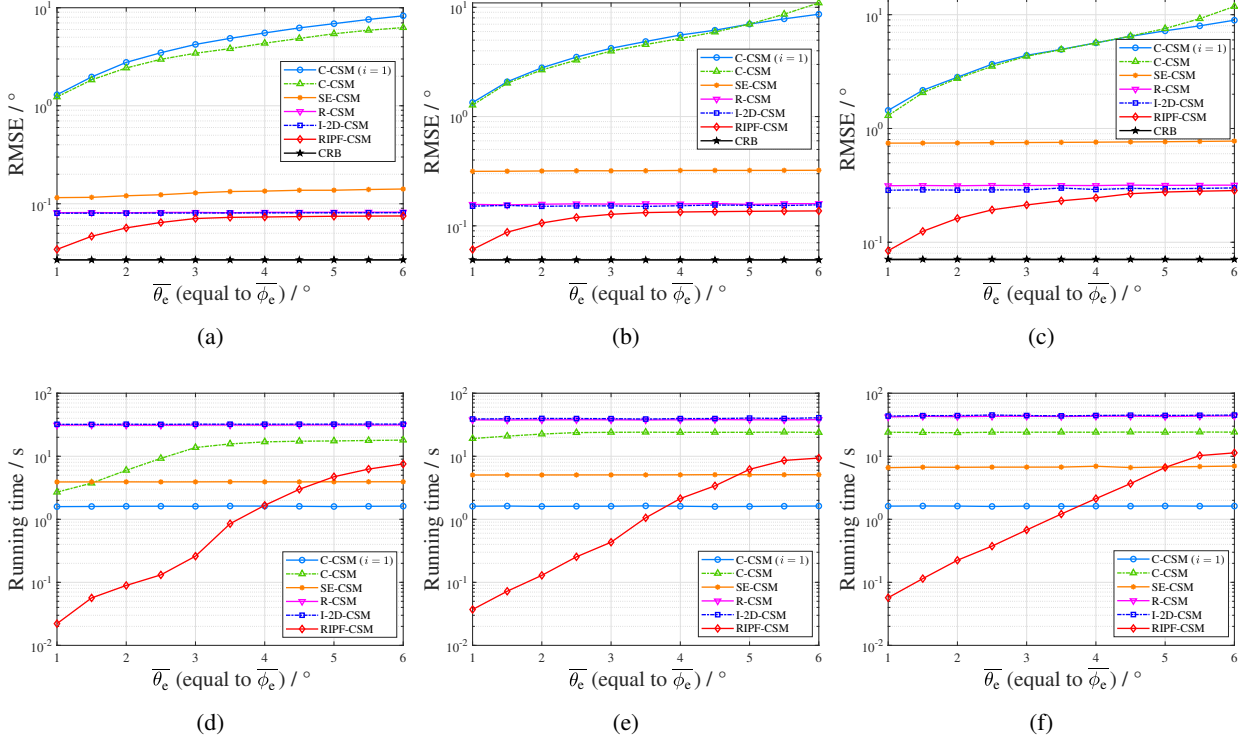


Fig. 4. RMSE of estimation results and running time in $\bar{\theta}_e, \bar{\phi}_e \in [1^\circ, 6^\circ]$. (a) and (d) are with $N=1$; (b) and (e) are with $N=2$; (c) and (f) are with $N=3$.

insensitive to the accuracy of pre-estimated DoAs. Furthermore, since the robustness intervals of RIPF-CSM become larger when $\bar{\theta}_e$ and $\bar{\phi}_e$ increase, the performance degrades to almost the same as that of R-CSM and I-2D-CSM as shown in Figs. 4 (a)-(c).

Figs. 4 (d)-(f) show that the running time of RIPF-CSM decreases approximately in the square order with the decrease of $\bar{\theta}_e$ and $\bar{\phi}_e$. Such phenomenon coincides with the expression in TABLE I that the radii of the robustness intervals as well as the number of iterations decrease when the pre-estimated DoAs are more accurate. On the contrary, it is observed that generally the running time of the benchmark methods cannot benefit from the pre-estimated DoAs even if they are accurate. It is due to the fact that C-CSM and SE-CSM are difficult to converge and often terminates at the maximum number of iterations, and the initial robustness intervals of R-CSM and I-2D-CSM are so large that $\bar{\theta}_e$ and $\bar{\phi}_e$ just slightly affect the estimation accuracy and thus the convergence speed. In Fig. 4 (d), although C-CSM can converge when pre-estimated DoAs are accurate enough, the high complexity from its focusing process and MUSIC algorithm leads to longer running time than RIPF-CSM. When $\bar{\theta}_e$ and $\bar{\phi}_e$ are not greater than 3.5° , the running time

TABLE III
RUNNING TIME WITH DIFFERENT SEARCH STEPS

N	$v_\theta (v_\phi) / ^\circ$	Running time / s					
		C-CSM ($i = 1$)	C-CSM	SE-CSM	R-CSM	I-2D-CSM	RIPF-CSM
1	1	0.09427	0.1398	0.1999	1.234	2.534	0.03244
	0.5	0.3007	0.8769	0.8687	4.747	11.10	0.07617
	0.2	1.607	13.75	3.924	31.25	32.21	0.2598
	0.1	6.335	88.17	17.39	125.9	131.3	0.8379
2	1	0.09507	0.2267	0.2068	1.625	3.296	0.04910
	0.5	0.3023	2.265	0.8766	6.240	15.05	0.09897
	0.2	1.612	23.98	5.062	37.84	39.48	0.4329
	0.1	6.352	94.51	19.75	156.3	162.8	1.400
3	1	0.09567	1.287	0.2154	1.755	3.648	0.06761
	0.5	0.3040	4.250	0.8855	6.779	18.02	0.1443
	0.2	1.617	24.04	6.722	43.11	44.22	0.6770
	0.1	6.370	94.75	19.88	175.8	180.5	2.560

TABLE IV
RUNNING TIME WITH DIFFERENT NUMBER OF FREQUENCY POINTS

N	Z	Running time / s					
		C-CSM ($i = 1$)	C-CSM	SE-CSM	R-CSM	I-2D-CSM	RIPF-CSM
1	32	1.607	13.75	3.924	31.25	32.21	0.2598
	64	1.623	10.66	3.941	55.55	57.13	0.3612
	128	1.635	8.536	3.949	108.2	112.5	0.5147
2	32	1.612	23.98	5.062	37.84	39.48	0.4329
	64	1.629	24.05	5.080	69.83	73.63	0.5918
	128	1.642	15.69	5.095	132.6	141.3	0.7834
3	32	1.617	24.04	6.722	43.11	44.22	0.6770
	64	1.634	24.14	6.745	76.74	81.64	0.8996
	128	1.649	24.28	6.756	144.3	156.2	1.227

of RIPF-CSM is shorter than other methods as illustrated in Figs. 4 (d)-(f), which exhibits the high efficiency contributed by the integration of the less candidate frequency points, the robustness intervals and the range-shrunk spatial spectrum. According to the above analysis, RIPF-CSM achieves a better trade-off between performance and complexity than the other methods when $\overline{\theta_e}, \overline{\phi_e} \in [1^\circ, 6^\circ]$ that are typical in practical scenarios.

D. Running Time Versus Search Steps and Number of Frequency Points

Note from TABLE I that the search steps v_θ and v_ϕ , and the number of frequency points Z severely affect the computational complexity of each method. To explicitly reveal such dependence, we measure the running time with different search steps and number of frequency points.

The results are respectively shown in TABLE III and TABLE IV.

It is observed from TABLE III that the reduction of v_θ and v_ϕ increases the running time of different methods, and their running time generally coincides with the complexity expressions in TABLE I. TABLE IV indicates that the running time of most methods increases with Z while C-CSM for $N = 1, 2$ enjoys a fast convergence speed and thus its computational complexity is reduced. Accordingly, the increase of Z is generally negative to the running speed, but it helps improve the accuracy of DoA estimation in each iteration so that the number of iterations required for convergence can be reduced. In addition, the results in TABLE IV also coincide with the complexity expressions of different methods in TABLE I.

Furthermore, in TABLE III and IV, the running time of RIPF-CSM is shorter than that of other methods for any v_θ , v_ϕ or Z , which demonstrates the high efficiency of RIPF-CSM. Besides, it is illustrated that the difference of the running time between RIPF-CSM and other benchmark methods increases with the decrease of search steps, so the efficiency advantage of RIPF-CSM enables it to be suitable for the applications that require high resolution of DoA estimation.

VI. CONCLUSION

In this paper, we propose RIPF-CSM for UCA-based MIMO systems to iteratively estimate the 2D DoAs of wideband signals. In the proposed method, the robustness intervals are proposed to obtain high focusing performance, and the efficiency of RIPF-CSM is guaranteed by shrinking the range of MUSIC spatial spectrum to the regions that are constrained by the robustness intervals and reducing the number of candidate frequency points which increases flexibly with iterations. Based on the previous estimated DoAs, the key parameters of RIPF-CSM in the current iteration are adjusted to improve the reliability. In addition, the computational complexity of RIPF-CSM is lower than benchmark CSM methods in practical scenarios. To show the performance of RIPF-CSM analytically, we derive the CRB of the 2D DoA estimation with UCA for multiple wideband signal sources with multiple snapshots. According to the derived CRB, we provide effective guidelines for practical applications. The simulation results reveal that RIPF-CSM outperforms the benchmark CSM methods, and its performance is also shown to be closer to CRB. Furthermore, RIPF-CSM is efficient under a variety of parameter settings, and its advantage in terms of complexity is obvious when the pre-estimated DoAs are accurate enough or the scenario requires high angle resolution.

APPENDIX A

DIMENSION EXTENSION OF SOME BENCHMARK METHODS

SE-CSM in [22], R-CSM in [25] and I-2D-CSM in [26] only consider 1D DoAs. For fair comparison, it is reasonable to extend them to the versions for 2D DoA estimation, where the key of the extension is the selection of the extra focusing angles. We give the corresponding rules for the three methods in 2D DoA estimation as follows.

1) *SE-CSM*:

In [22], the extra focusing angles in the first iteration are set as $\hat{\theta}_n^{(0)} \pm 0.25\text{BW}_\theta$, where BW_θ denotes the vertical 3dB beamwidth and $n = 1, 2, \dots, \hat{N}_{i-1}$. In the subsequent iterations, the extra focusing angles are set to be $\hat{\theta}_n^{(i-1)} \pm 0.125\text{BW}_\theta$.

Following this idea, in the extended 2D DoA estimation, the extra focusing angles in the first iteration are set as $(\hat{\theta}_n^{(0)} \pm 0.25\text{BW}_\theta, \hat{\phi}_n^{(0)} \pm 0.25\text{BW}_\phi)$, and the extra angles in subsequent iterations are set as $(\hat{\theta}_n^{(i-1)} \pm 0.125\text{BW}_\theta, \hat{\phi}_n^{(i-1)} \pm 0.125\text{BW}_\phi)$. Since the beamwidth of UCA varies with different elevation angles [39], BW_θ and BW_ϕ respectively stand for the vertical and horizontal 3dB beamwidth of the quiescent array pattern [40] in this work when the direction of the beam is at $(0^\circ, 0^\circ)$.

2) *R-CSM*:

The extra focusing angles in the i -th iteration of R-CSM in [25] are obtained by sampling the elevation robustness interval $\mathbb{G}_n^{\theta'}(i)$ which is expressed as:

$$\mathbb{G}_n^{\theta'}(i) = \left[\arcsin \left(\max \left[0, \sin \hat{\theta}_n^{(i-1)} - \frac{1}{2i^p} \right] \right), \arcsin \left(\min \left[\sin \hat{\theta}_n^{(i-1)} + \frac{1}{2i^p}, 1 \right] \right) \right], \quad (37)$$

where $n=1, 2, \dots, \hat{N}_{i-1}$, $p = 2$, and its radius is $R_n^{\theta'}(i)$ as defined in Section III-B. Considering $1/(2i^p)$ in (37) as the radius of the interval mapped from $\mathbb{G}_n^{\theta'}(i)$ by \sin whose codomain is $[0, 1]$ with $\theta \in [0^\circ, 90^\circ]$, the radius for an azimuth interval mapped by \sin is meaningless since $\phi \in [0^\circ, 360^\circ)$ thus the mapping is no longer injective. In this sense, the radius of the azimuth robustness interval is set in angle domain, i.e., $R_n^{\phi'}(i) = 360^\circ/(2i^p)$. The azimuth robustness interval $\mathbb{G}_n^{\phi'}(i)$ is obtained by replacing $R_n^{\phi}(i)$ with $R_n^{\phi'}(i)$ in (12).

3) *I-2D-CSM*:

The elevation robustness interval of I-2D-CSM in [26] is similar to that of R-CSM, from which extra focusing angles are sampled. The interval is expressed as:

$$\mathbb{G}_n^{\theta''}(i) = \left[\arcsin \left(\max \left[0, \sin \hat{\theta}_n^{(i-1)} - \frac{1}{2 \min[i, i_s^\theta]^2} \right] \right), \arcsin \left(\min \left[\sin \hat{\theta}_n^{(i-1)} + \frac{1}{2 \min[i, i_s^\theta]^2}, 1 \right] \right) \right], \quad (38)$$

where $n = 1, 2, \dots, \hat{N}_{i-1}$, $i_s^\theta = \rho v_\theta / 1^\circ$, $\rho \in (1, 3]$, and its radius is $R_n^{\theta''}(i)$ as defined in Section III-B. In this paper, ρ is set as 2. By imitating the dimension extension of the above R-CSM, the radius of the azimuth robustness interval in the i -th iteration is set as $R_n^{\phi''}(i) = 360^\circ / (2 \min[i, i_s^\phi]^2)$ where $i_s^\phi = \rho v_\phi / 1^\circ$. The azimuth robustness interval $\mathbb{G}_n^{\phi''}(i)$ can be obtained by replacing $R_n^\phi(i)$ with $R_n^{\phi''}(i)$ in (12).

APPENDIX B

PARAMETER CONSTRAINT DERIVATION FOR RIPF-CSM WITH LOWER COMPUTATIONAL COMPLEXITY THAN C-CSM IN A SINGLE ITERATION

To guarantee the lower computational complexity of RIPF-CSM when compared with C-CSM in a single iteration, the parameters mentioned in TABLE I should satisfy one constraint that can be easily achieved and is discussed as follows.

The constraint is derived on the premise of the following two assumptions, which are generally the cases in practice [25]. First, the changes of the results between adjacent iterations are large only in the first few iterations, and the changes are smaller in the subsequent iterations. Statistically, these small changes appear more frequently than the large ones as shown in [25] and in our results. Based on these arguments, it is reasonable to assume $d_{\bar{\delta}}^{(i)}$ in (9), $i = 1, 2, \dots, I_c$, follows a certain exponential distribution. Second, considering estimation results generally keep approaching the actual DoAs with iterations, and the final estimation errors are close to zero, we assume $d_{\bar{\delta}}^{(i)}$ satisfies:

$$\sum_{i=1}^{I_c} d_{\bar{\delta}}^{(i)} = \frac{d_\theta + d_\phi}{2}, \quad (39)$$

where I_c denotes the number of iterations required for termination.

Based on the above assumptions, we give the following derivation. By combining (9), (10) and (39), there exists:

$$Z_{\text{in}}^{(i)} \leq 1 + \frac{(d_\theta + d_\phi) [(d_\theta + d_\phi)I + 2Z]}{4I_c I}. \quad (40)$$

Furthermore, we have $\mathcal{E}[d_{\bar{\delta}}^{(i)}] = (d_\theta + d_\phi) / (2I_c)$ from (39). It is known from $\hat{\theta}_n^{(i)} \in [0^\circ, 90^\circ]$ that $\max[(b - \sin \hat{\theta}_n^{(i)})(b - \cos \hat{\theta}_n^{(i)})] = b(b - 1)$. According to the above equation, $i \geq 1$, (13), (14), $\mathcal{E}[d_{\bar{\delta}}^{(i)}]$ and the cumulative distribution function of exponential distribution, $\sum_{n=1}^{\hat{N}_i} R_n^\theta(i) R_n^\phi(i)$ satisfies:

$$\mathcal{P} \left[\sum_{n=1}^{\hat{N}_i} R_n^\theta(i) R_n^\phi(i) < \left(\frac{\ln 100}{2I_c} \right)^2 \hat{N}_i \overline{\theta_e} \overline{\phi_e} (d_\theta + d_\phi)^2 b(b - 1) \right] \leq 99\%. \quad (41)$$

On the basis of TABLE I, when the computational complexity of RIPF-CSM is lower than that of C-CSM in a single iteration, the following inequality is satisfied:

$$Z_{\text{in}}^{(i)} \left[M + 8K_f + 16 \sum_{n=1}^{\hat{N}_i} R_n^\theta(i) R_n^\phi(i) / (v_\theta v_\phi) \right] < Z(M + 4\hat{N}_i + 8K_f) + 4L_\theta L_\phi. \quad (42)$$

By substituting the right expression of (40) and the right expression in the $\mathcal{P}[\cdot]$ of (41) into $Z_{\text{in}}^{(i)}$ and $\sum_{n=1}^{\hat{N}_i} R_n^\theta(i) R_n^\phi(i)$ in (42) respectively, the probability that the computational complexity of RIPF-CSM in a single iteration is less than that of C-CSM is up to 99%. In practical scenarios, such constraint is easily to be satisfied by most of the simulation parameters in Section V, e.g., the default simulation parameters with $I_c = 5$ which is a general number of iterations as mentioned in Section III-B. With such high probability, it is reasonable to regard that RIPF-CSM enjoys the lower computational complexity than that of C-CSM in a single iteration.

APPENDIX C

DERIVATION OF THE FISHER INFORMATION MATRIX

Lemma 1: Suppose $k_1, k_2 \in \{1, 2, \dots, K_f\}$ and $z_1, z_2 \in \{1, 2, \dots, Z\}$, then:

$$\mathcal{E} [\mathbf{w}^H(k_1, f_{z_1}) \mathbf{w}(k_1, f_{z_1}) \mathbf{w}^H(k_2, f_{z_2}) \mathbf{w}(k_2, f_{z_2})] = \begin{cases} M(M+1) Z^2 \sigma^4, & \text{if } k_1 = k_2 \text{ and } z_1 = z_2, \\ M^2 Z^2 \sigma^4, & \text{otherwise,} \end{cases} \quad (43)$$

$$\mathcal{E} [\mathbf{w}^H(k_1, f_{z_1}) \mathbf{w}(k_1, f_{z_1}) \mathbf{w}^T(k_2, f_{z_2})] = 0. \quad (44)$$

Proof: This lemma can be easily obtained based on the correlation properties of white Gaussian noise.

Derivation of the Fisher information matrix:

Denote $d_{\sigma^2} = \partial \ln P / \partial \sigma^2$, $\mathbf{d}_{\hat{\mathbf{s}}_f}^{k,z} = \partial \ln P / \partial \hat{\mathbf{s}}_f(k, f_z)$, $\mathbf{d}_{\hat{\mathbf{s}}_f}^{k,z} = \partial \ln P / \partial \hat{\mathbf{s}}_f(k, f_z)$ and $\mathbf{d}_\zeta = \partial \ln P / \partial \zeta$. They are respectively calculated as:

$$d_{\sigma^2} = -\frac{K_f M Z}{\sigma^2} + \frac{1}{Z \sigma^4} \sum_{k=1}^{K_f} \sum_{z=1}^Z \mathbf{w}^H(k, f_z) \mathbf{w}(k, f_z), \quad (45)$$

$$\mathbf{d}_{\hat{\mathbf{s}}_f}^{k,z} = \frac{2}{Z \sigma^2} \text{Re} [\mathbf{A}^H(f_z) \mathbf{w}(k, f_z)], \quad (46)$$

$$\mathbf{d}_{\hat{\mathbf{s}}_f}^{k,z} = \frac{2}{Z \sigma^2} \text{Im} [\mathbf{A}^H(f_z) \mathbf{w}(k, f_z)], \quad (47)$$

$$\mathbf{d}_\zeta = \frac{2}{Z \sigma^2} \sum_{k=1}^{K_f} \sum_{z=1}^Z \text{Re} [\mathbf{\Xi}^H(k, f_z) \mathbf{D}^H(f_z) \mathbf{w}(k, f_z)]. \quad (48)$$

Based on (45)-(48) and Lemma 1, we have:

$$\mathcal{E} [(d_{\sigma^2})^2] = \frac{K_f M Z}{\sigma^4}, \quad (49)$$

$$\mathcal{E} [d_{\sigma^2} \mathbf{d}_{\mathbf{s}_f}^{k,z}] = \mathcal{E} [d_{\sigma^2} \mathbf{d}_{\mathbf{s}_f}^{k,z}] = \mathcal{E} [d_{\sigma^2} \mathbf{d}_{\zeta}] = 0, \quad (50)$$

$$\mathcal{E} [\mathbf{d}_{\mathbf{s}_f}^{k,z} \mathbf{d}_{\zeta}^T] = \frac{2}{Z\sigma^2} \text{Re} [\mathbf{A}^H(f_z) \mathbf{D}(f_z) \mathbf{\Xi}(k, f_z)], \quad (51)$$

$$\mathcal{E} [\mathbf{d}_{\mathbf{s}_f}^{k,z} \mathbf{d}_{\zeta}^T] = \frac{2}{Z\sigma^2} \text{Im} [\mathbf{A}^H(f_z) \mathbf{D}(f_z) \mathbf{\Xi}(k, f_z)], \quad (52)$$

$$\mathcal{E} [\mathbf{d}_{\zeta} \mathbf{d}_{\zeta}^T] = \frac{2}{Z\sigma^2} \sum_{k=1}^{K_f} \sum_{z=1}^Z \text{Re} [\mathbf{\Xi}^H(k, f_z) \mathbf{D}^H(f_z) \mathbf{D}(f_z) \mathbf{\Xi}(k, f_z)], \quad (53)$$

$$\mathcal{E} [\mathbf{d}_{\mathbf{s}_f}^{k_1,z_1} \mathbf{d}_{\mathbf{s}_f}^{k_2,z_2 T}] = \mathcal{E} [\mathbf{d}_{\mathbf{s}_f}^{k_1,z_1} \mathbf{d}_{\mathbf{s}_f}^{k_2,z_2 T}] = \begin{cases} \frac{2}{Z\sigma^2} \text{Re} [\mathbf{A}^H(f_{z_1}) \mathbf{A}(f_{z_2})], & \text{if } k_1 = k_2 \text{ and } z_1 = z_2, \\ 0, & \text{otherwise,} \end{cases} \quad (54)$$

$$\mathcal{E} [\mathbf{d}_{\mathbf{s}_f}^{k_1,z_1} \mathbf{d}_{\mathbf{s}_f}^{k_2,z_2 T}] = -\mathcal{E} [\mathbf{d}_{\mathbf{s}_f}^{k_1,z_1} \mathbf{d}_{\mathbf{s}_f}^{k_2,z_2 T}] = \begin{cases} -\frac{2}{Z\sigma^2} \text{Im} [\mathbf{A}^H(f_{z_1}) \mathbf{A}(f_{z_2})], & \text{if } k_1 = k_2 \text{ and } z_1 = z_2, \\ 0, & \text{otherwise,} \end{cases} \quad (55)$$

where $k, k_1, k_2 \in \{1, 2, \dots, K_f\}$ and $z, z_1, z_2 \in \{1, 2, \dots, Z\}$. Then, (20) can be obtained by substituting (49)-(55) into $\mathbf{F} = \mathcal{E}[\psi\psi^T]$ which is mentioned in Section IV-A.

REFERENCES

- [1] Y. Jeon, G. -T. Gil and Y. H. Lee, "Design and analysis of LoS-MIMO systems with uniform circular arrays," in *IEEE Trans. Wireless Commun.*, vol. 20, no. 7, pp. 4527-4540, Jul. 2021.
- [2] A. A. Abdallah and Z. M. Kassas, "Multipath Mitigation via Synthetic Aperture Beamforming for Indoor and Deep Urban Navigation," in *IEEE Trans. Veh. Technol.*, vol. 70, no. 9, pp. 8838-8853, Sep. 2021.
- [3] Z. Zheng, W. -Q. Wang, H. Meng, H. C. So and H. Zhang, "Efficient beamspace-based algorithm for two-dimensional DOA estimation of incoherently distributed sources in massive MIMO systems," in *IEEE Trans. Veh. Technol.*, vol. 67, no. 12, pp. 11776-11789, Dec. 2018.
- [4] M. H. Dinan, N. S. Perović and M. F. Flanagan, "Sparse layered MIMO with iterative detection," in *IEEE Trans. Commun.*, vol. 70, no. 3, pp. 2042-2056, Mar. 2022.
- [5] P. Ioannides and C. A. Balanis, "Uniform circular arrays for smart antennas," in *IEEE Antennas Propag. Mag.*, vol. 47, no. 4, pp. 192-206, Aug. 2005.
- [6] X. Cai and W. Fan, "A complexity-efficient high resolution propagation parameter estimation algorithm for ultra-wideband large-scale uniform circular array," in *IEEE Trans. Commun.*, vol. 67, no. 8, pp. 5862-5874, Aug. 2019.
- [7] D. He, X. Chen, L. Pei, F. Zhu, L. Jiang and W. Yu, "Multi-BS spatial spectrum fusion for 2-D DOA estimation and localization using UCA in massive MIMO system," in *IEEE Trans. Instrum. Meas.*, vol. 70, pp. 1-13, 2021.
- [8] X. Zhang, G. Liao, Z. Yang and Y. Chen, "Derivative ESPRIT for DOA and polarization estimation for UCA using tangential individually-polarized dipole," in *Digit. Signal Process.*, vol. 96, pp. 1-10, Jan. 2020.

- [9] D. Hu, Y. Zhang, L. He and J. Wu, "Low-complexity deep-learning-based DOA estimation for hybrid massive MIMO systems with uniform circular arrays," in *IEEE Wireless Commun. Lett.*, vol. 9, no. 1, pp. 83-86, Jan. 2020.
- [10] A. Barthelme and W. Utschick, "DoA Estimation Using Neural Network-Based Covariance Matrix Reconstruction," in *IEEE Signal Process. Lett.*, vol. 28, pp. 783-787, 2021.
- [11] A. Barthelme and W. Utschick, "A machine learning approach to DoA estimation and model order selection for antenna arrays with subarray sampling," in *IEEE Trans. Signal Process.*, vol. 69, pp. 3075-3087, 2021.
- [12] P. Stoica and A. Nehorai, "MUSIC, maximum likelihood, and Cramer-Rao bound," in *IEEE Trans. Acoust., Speech, Signal Process.*, vol. 37, no. 5, pp. 720-741, May 1989.
- [13] P. Vallet, X. Mestre, and P. Loubaton, "Performance analysis of an improved MUSIC DoA estimator," in *IEEE Trans. Signal Process.*, vol. 63, no. 23, pp. 6407-6422, Dec. 2015.
- [14] Y. Hu, T. D. Abhayapala and P. N. Samarasinghe, "Multiple source direction of arrival estimations using relative sound pressure based MUSIC," in *IEEE/ACM Trans. Audio, Speech, Lang. Process.*, vol. 29, pp. 253-264, 2021.
- [15] M. Wax, T. -J. Shan, and T. Kailath, "Spatio-temporal spectral analysis by eigenstructure methods," in *IEEE Trans. Acoust., Speech, Signal Process.*, vol. 32, no. 4, pp. 817-827, Aug. 1984.
- [16] L. Wang, L. Zhao, G. Bi, C. Wan, L. Zhang and H. Zhang, "Novel wideband DOA estimation based on sparse bayesian learning with dirichlet process priors," in *IEEE Trans. Signal Process.*, vol. 64, no. 2, pp. 275-289, Jan. 2016.
- [17] Q. Shen, W. Cui, and W. Liu, "Underdetermined wideband DOA estimation of off-grid sources employing the difference co-array concept," in *Signal Process.*, vol. 130, pp. 299-304, Jan. 2017.
- [18] M. A. Doron, E. Doron, and A. J. Weiss, "Coherent wide-band processing for arbitrary array geometry," in *IEEE Trans. Signal Process.*, vol. 41, no. 1, pp. 414-417, Jan. 1993.
- [19] Y. Pan, G. Q. Luo, Z. Liao, B. Cai, and M. Yao, "Wideband direction-of-arrival estimation with arbitrary array via coherent annihilating," in *IEEE Access*, vol. 7, pp. 51058-51068, 2019.
- [20] F. Wang, Z. Tian, G. Leus and J. Fang, "Direction of arrival estimation of wideband sources using sparse linear arrays," in *IEEE Trans. Signal Process.*, vol. 69, pp. 4444-4457, 2021.
- [21] H. Wang and M. Kaveh, "Coherent signal-subspace processing for the detection and estimation of angles of arrival of multiple wide-band sources," in *IEEE Trans. Acoust., Speech, Signal Process.*, vol. 33, no. 4, pp. 823-831, Aug. 1985.
- [22] H. Hung and M. Kaveh, "Focussing matrices for coherent signal-subspace processing," in *IEEE Trans. Acoust., Speech, Signal Process.*, vol. 36, no. 8, pp. 1272-1281, Aug. 1988.
- [23] M. A. Doron and A. J. Weiss, "On focusing matrices for wide-band array processing," in *IEEE Trans. Signal Process.*, vol. 40, no. 6, pp. 1295-1302, Jun. 1992.
- [24] S. Valaee and P. Kabal, "Wideband array processing using a two-sided correlation transformation," in *IEEE Trans. Signal Process.*, vol. 43, no. 1, pp. 160-172, Jan. 1995.
- [25] F. Sellone, "Robust auto-focusing wideband DOA estimation," in *Signal Process.*, vol. 86, no. 1, pp. 17-37, Jan. 2006.
- [26] F. Wang, X. Cui and M. Lu, "A new iterative coherent subspace method for wideband direction finding," in *Proc. 2015 IEEE Int. Radar Conf.*, Arlington, VA, USA, May 2015, pp. 0405-0410.
- [27] H. Fu, S. Abeywickrama, C. Yuen and M. Zhang, "Robust phase-ambiguity-immune DOA estimation scheme for antenna array," in *IEEE Trans. Veh. Technol.*, vol. 68, no. 7, pp. 6686-6696, Jul. 2019.
- [28] F. Wen, P. Liu, H. Wei, Y. Zhang and R. C. Qiu, "Joint azimuth, elevation, and delay estimation for 3-D indoor localization," in *IEEE Trans. Veh. Technol.*, vol. 67, no. 5, pp. 4248-4261, May 2018.
- [29] J. Huang, C. Liu, W. Hu and K. Liao, "Design of a grating lobes-free architecture for distributed sensor system with arbitrary element spacing," in *Remote Sens.*, vol. 14, no. 6, pp.1356-1380, Mar. 2022.
- [30] Y. Shi, S. Wang and Z. Huang, "An algorithm for UCA sources parameter estimate based on multistage Wiener filters,"

- in *Proc. 3th IEEE Int. Conf. Netw., Sens. Control (ICNSC)*, Ft. Lauderdale, FL, USA, Apr. 2006, pp. 993-996.
- [31] H. Cox, R. Zeskind and M. Owen, "Robust adaptive beamforming," in *IEEE Trans. Acoust., Speech, Signal Process.*, vol. 35, no. 10, pp. 1365–1376, Oct. 1987.
 - [32] F. Liu, C. Masouros, A. P. Petropulu, H. Griffiths and L. Hanzo, "Joint radar and communication design: applications, state-of-the-art, and the road ahead," in *IEEE Trans. Commun.*, vol. 68, no. 6, pp. 3834–3862, Jun. 2020.
 - [33] N. Singh, L. H. Son, F. Chiclana, and J.-P. Magnot, "A new fusion of salp swarm with sine cosine for optimization of non-linear functions," in *Eng. Comput.*, vol. 36, no. 1, pp. 185–212, Jan. 2020.
 - [34] X. Li, S. Wang, Y. Wang and Y. Cai, "Tutorial: complexity analysis of singular value decomposition and its variants," 2019, *arXiv:1906.12085v3*. [Online]. Available: <http://arxiv.org/abs/1906.12085v3>
 - [35] Y. Zheng and Y. Liang, "Eigenvalue-based spectrum sensing algorithms for cognitive radio," in *IEEE Trans. Commun.*, vol. 57, no. 6, pp. 1784–1793, Jun. 2009.
 - [36] B. Xu and Y. Zhao, "Transmit beamspace-based DOD and DOA estimation method for bistatic MIMO radar," in *Signal Process.*, vol. 157, pp. 88-96, Apr. 2019.
 - [37] L. Wan, Y. Sun, L. Sun, Z. Ning and J. J. P. C. Rodrigues, "Deep learning based autonomous vehicle super resolution DOA estimation for safety driving," in *IEEE Trans. Intell. Transp. Syst.*, vol. 22, no. 7, pp. 4301-4315, Jul. 2021.
 - [38] S. Wang, K. Nie, M. He and Y. He, "DOA estimation aided by magnitude measurements," in *IEEE Trans. Veh. Technol.*, vol. 70, no. 11, pp. 12197-12202, Nov. 2021.
 - [39] H. Tang, X. Zhong and Z. Nie, "On the approximate calculation of half-power beam width for uniform circular arrays," in *ACES Journal*, vol. 34, no. 3, pp. 444-450, Mar. 2019.
 - [40] L. Griffiths and K. Buckley, "Quiescent pattern control in linearly constrained adaptive arrays," in *IEEE Trans. Aerosp. Electron. Syst.*, vol. 35, no. 7, pp. 917-926, Jul. 1987.